Electron beam

Beaker epitaxy

$\gamma\text{-Fe}_2\text{O}_3$
$\text{Fe}_{2-x}\text{Ni}_x\text{O}_3$
$\text{Ni}_{1-x}\text{Fe}_x$
Ni

ADT

Ni@ γ-Fe$_2$O$_3$ superparticle

Hierachical Ni@Fe$_2$O$_3$ superparticles through epitaxial growth of γ-Fe$_2$O$_3$ nanorods on *in situ* formed Ni nanoplates

We report the solution synthesis of magnetic nanocomposites with complex but well-defined mesoscopic architectures through "beaker epitaxy". Electron crystallography revealed that the buffer layer at the interface between the metal "support" and the metal oxide nanorods can be fine-tuned by "alloying" the metal components to achieve a match between the lattice parameters of the metal substrate and the metal oxide nanorods. The miscibility of the transition metals allows the buffer layer approach to be generalized for the synthesis of magnetic nanocomposites.

As featured in:
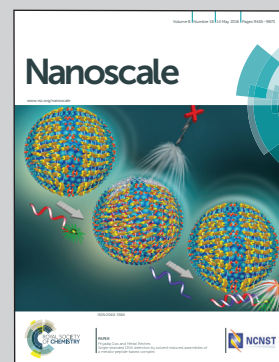
Nanoscale

ROYAL SOCIETY OF CHEMISTRY

www.rsc.org/nanoscale

Nanoscale

Hierachical Ni@Fe₂O₃ superparticles through epitaxial growth of γ-Fe₂O₃ nanorods on *in situ* formed Ni nanoplates†

Muhammad Nawaz Tahir,*[a] Jana Herzberger,[b,c] Filipe Natalio,‡[a] Oskar Köhler,[a] Robert Branscheid,[d] Enrico Mugnaioli,[d] Vadim Ksenofontov,[a] Martin Panthöfer,[a] Ute Kolb,[d] Holger Frey[b] and Wolfgang Tremel*[a]

One endeavour of nanochemistry is the bottom-up synthesis of functional mesoscale structures from basic building blocks. We report a one-pot wet chemical synthesis of Ni@γ-Fe₂O₃ superparticles containing Ni cores densely covered with highly oriented γ-Fe₂O₃ (maghemite) nanorods (NRs) by controlled reduction/decomposition of nickel acetate (Ni(ac)₂) and Fe(CO)₅. Automated diffraction tomography (ADT) of the Ni–Fe₂O₃ interface in combination with Mössbauer spectroscopy showed that selective and oriented growth of the γ-Fe₂O₃ nanorods on the Ni core is facilitated through the formation of a Fe₀.₀₅Ni₀.₉₅ alloy and the appearance of superstructure features that may reduce strain at the Ni–Fe₂O₃ interface. The common orientation of the maghemite nanorods on the Ni core of the superparticles leads to a greatly enhanced magnetization. After functionalization with a catechol-functional polyethylene glycol (C-PEG) ligand the Ni@γ-Fe₂O₃ superparticles were dispersible in water.

Introduction

Nano-heterostructures containing chemically distinct components have great potential for advancing nanomaterial research by providing a means to define diverse functionalities within single nanoparticles.[1] Moreover, new properties that do

*[a]Institut für Anorganische Chemie und Analytische Chemie der Johannes Gutenberg-Universität, Duesbergweg 10-14, D-55099 Mainz, Germany.
E-mail: tahir@uni-mainz.de, tremel@uni-mainz.de*
[b]Institut für Organische Chemie, Johannes-Gutenberg-Universität, Duesbergweg 10-14, D-55099 Mainz, Germany
[c]Graduate School Materials Science in Mainz, Staudinger Weg 9, 55128 Mainz, Germany
[d]Institut für Physikalische Chemie, Johannes-Gutenberg-Universität, Welderweg 15, D-55099 Mainz, Germany

not exist in the individual components may arise from strong interfacial interactions at the nanoscale. In recent years, some progress has been made concerning the fabrication of nano-composites with spherical,[2] coaxial core–shell,[3] or one- and two-dimensional (1D and 2D) heterojunction structures.[4–6] To explore potential applications, architecturally assembling of primary nano-building blocks into specific geometric forms is needed. However, despite a few reported hierarchical com complex structures[7–13] a general scheme for the controlled organization and the preferential crystallographic orientation of the secondary structure is lacking.

Therefore it would be desirable to obtain nanostructured materials, where the individual units, each of them characterized by its particular physical properties, surface chemistry and morphology, can be combined into a single nano-object. In the realm of nanostructures there are examples of architectures based on inorganic materials, such as nanowire superlattices,[14] or multi-layered nanowires.[15,16] A central target of colloidal nanocrystal research is to create similar – or even more complex – structures while leveraging the advantages of solution-phase fabrication, such as low-cost synthesis and compatibility in disparate environments. Important fundamental components could be catalytically active metals like Ni,[17] Pd[18] or Pt[19] and magnetic metal oxides like Fe₂O₃[20] or Fe₃O₄.[19]

The chemical functionality of the individual components allows studying the assembly of such hetero-nanostructures.[21]

Multicomponent core@shell,[22] yolk@shell[23] or phase-segregated heterodimer[24,25] particles or materials containing metal and magnetic metal oxide components with different compositions like Pt@Fe$_3$O$_4$,[26] Au@Fe$_3$O$_4$,[27–29] FePt@MnO,[30] Ag@Fe$_3$O$_4$,[31] Au@MnO[32] or Au@MnO@SiO$_2$[33] have attracted particular attention. The synthesis of these hetero-nanoparticles is facilitated when the interfacial energy is reduced by epitaxial growth, *i.e.*, an extremely thin metallic interlayer forming at the interface, because the two components have similar lattice parameters.[34–37] The synthesis of nanoparticles by thermolysis of organometallic precursors in the presence of surfactants is a unique tool to control the kinetics of phase equilibria and particle aggregation, because phase formation and ordering of the components at the nanoscale are under molecular control. They depend on (i) the decomposition temperatures of the precursors, (ii) the relative activation energies for nucleation, and (iii) interfacial energies which are dictated by interactions of the surfactant and the solvents with the particle surfaces. Despite tremendous efforts to find a general synthetic access to such heterostructures, it still remains a challenge to prepare nanoparticles with complex structures *e.g.* superparticles having well-controlled sizes, shapes, compositions, and properties. To the best of our knowledge there is no report for the synthesis of superparticles using colloidal protocols. We have demonstrated the relevance of the precursor decomposition temperature by the selective synthesis of nanocrystals of the ternary compounds CoFe$_2$O$_4$, CuFe$_2$O$_4$ and phase segregated Co@Fe$_2$O$_3$ and Cu@Fe$_3$O$_4$ heteroparticles.[17,20,38] Based on these findings, we report here the controlled synthesis of colloidal hetero-superparticles consisting of nanoplates densely decorated with highly oriented maghemite (γ-Fe$_2$O$_3$, defect spinel) nanorods. Typically, particles in the size range of ~200 nm are difficult to solubilize (*e.g.* using low molecular weight C-PEGs). The catechol moiety is an excellent anchor group for high-valent metal oxide surfaces,[39–41] and in combination with PEG ensures excellent solubility of the superparticles in aqueous media. The commonly used established procedures to obtain catechol-functional PEGs are based on coupling chemistry, starting from a dopamine derivative and commercially available functional PEGs, *e.g.* NH$_2$-PEG or NHS-PEG,[42–44] but the palette of commercial PEGs with specific end-groups and different molecular weights is limited and can be high-priced. Therefore we use a new synthetic procedure for catechol-functional PEGs based on anionic ring opening polymerization of ethylene oxide (EO) starting from a protected catechol-initiator. This synthetic strategy allows precisely tailoring the chain-length of PEG through the initiator to monomer ratio and guarantees well-defined polymers through the living character of the polymerization. Further, additional functional groups could easily be introduced by various terminating agents or by incorporation of functional epoxides.[45,46] The as-synthesized superparticles could be solubilized after functionalization with a new catechol-polyethylene glycol (C-PEG) polymer ligand.[47] After functionalization the superparticles formed stable dispersions in a range of solvents including water.

Experimental

Materials

Iron(0) pentacarbonyl (Fe(CO)$_5$, 99.5%, Acros), nickel(II) acetate tetrahydrate (Ni(ac)$_2$·4H$_2$O, 99%, Fluka), oleic acid (Aldrich), oleylamine (80–90%, Acros), trioctylphosphine ([CH$_3$(CH$_2$)$_7$]$_3$P, 99% Sigma-Aldrich), ethanol (99.8%, Roth), toluene (>99%, Aldrich), hexane (p.A. Fisher), dichloromethane DCM (p.A. Fisher), dimethylformamide (DMF) (extra dry, >99.8%, Acros), diethyl ether (p.A. Fisher) were used as received without further purification.

Polymer synthesis

Ethylene oxide (99.5%) was purchased from Aldrich and hydrochloric acid (37%) from VWR chemicals. Chloroform-*d* was purchased from Deutero GmbH. All other solvents and reagents were ordered from Acros Organics.

Synthesis of Ni@γ-Fe$_2$O$_3$ superparticles

Hierarchically decorated Ni@γ-Fe$_2$O$_3$ superparticles were synthesized by mixing 62.25 mg (0.25 mmol) of nickel acetate Ni(ac)$_2$, 7 mL of oleylamine, 1 mmol of trioctyl-phosphine, and 2 mmol of oleic acid and stirring them for 20 min under the inert condition before increasing the temperature. The mixture was heated to 120 °C for 20 min. Subsequently, 67.55 μL of Fe(CO)$_5$ were added and the solution was heated 180 °C for 30 min and cooled slowly to room temperature. A black product was precipitated from the solution by adding an excess of ethanol. The precipitate was separated by centrifugation (9000 rpm, 10 min, RT). Finally, the product was dissolved in toluene, flushed with argon (Ar) and stored at +4 °C.

Synthesis of catechol initiated PEG by anionic ring opening polymerization of ethylene oxide (CA-PEG)

The synthesis of catechol-initiated PEG (CA-PEG) was performed as described recently.[47] Under argon atmosphere, 2,2-dimethyl-1,3-benzodioxole-5-propanol (catechol-acetonide-OH, CA-OH) (1 eq., 136.9 mg, 0.66 mmol) and cesium hydroxide (CsOH·1H$_2$O) (0.8 eq., 87.9 mg, 0.53 mmol) were suspended in 10 mL of benzene and heated to 60 °C for 30 min. Subsequently, the partially deprotonated initiator was evacuated at 55 °C for 12 h. About 15 mL of dry THF (stored over sodium) were cryo-transferred into the flask followed by the addition of 5 mL of DMSO by a syringe. The mixture was stirred for 15 min at room temperature to ensure complete dissolution of the cesium alkoxide, followed by cooling the flask to −80 °C. 2 mL of ethylene oxide (67 eq., 44 mmol) were cryo-transferred into the flask *via* a graduated ampoule. The polymerization proceeded for 12 h (55 °C) and was stopped by addition of 0.5 mL methanol. The polymer was precipitated into ice cold diethyl ether and separated by a centrifuge, yielding CA-PEG in a quantitative yield.

^{1}H NMR (C*D*Cl$_3$, 400 MHz): δ (C*H*Cl$_3$ = 7.26 ppm) 6.63–6.56 (m, 3 H, H_{arom}), 3.82–3.41 (m, backbone and C*H$_2$*–O–PEG), 2.57 (t, 2 H, C*H$_{2,benzyl}$*), 1.88–1.79 (m, 2 H, C*H$_2$*), 1.65 (s, 6 H, C*H$_3$*).

Deprotection of the acetonide group (C-PEG)

According to ref. 47, 100 mg of CA-PEG were dissolved in 5 mL of aqueous hydrochloric acid (1 mol L) and stirred for 12 h, letting the cleaved acetone escape. The solvent was removed under reduced pressure (10^{-3} mbar), and the polymer was dissolved in methanol, precipitated into ice cold diethyl ether and separated by a centrifuge. The yield was quantitative.

^{1}H NMR (methanol-d_4, 400 MHz): δ (MeOH = 3.31 ppm, 4.87 ppm) 6.67–6.62 (m, 2 H, HO–C–CH_{arom}), 6.51–6.48 (m, 1 H, CH_{arom}), 3.82–3.41 (m, backbone and CH_2–O-PEG), 2.53 (t, 2 H, C$H_{2,benzyl}$), 1.84–1.78 (m, 2 H, CH_2).

Surface functionalization of Ni@γ-Fe$_2$O$_3$ superparticles with CA-PEG

20 mg of Ni@γ-Fe$_2$O$_3$ superparticles dispersed in 20 mL of chloroform were dropped slowly over 1 h into the above synthesized polymer solution (40 mg/10 mL, of chloroform). The reaction was continuously stirred at room temperature for 5 h under inert conditions. The functionalized nanoparticles were precipitated by addition of hexane (90 mL) und separated from unbound polymer and surfactants by centrifugation. The Ni@γ-Fe$_2$O$_3$ superparticles were washed twice by dispersing them in a mixture of chloroform, hexane (1 : 3) and by phase transferring into water.

Physical characterization

Electron microscopy. The size and morphology of the as-synthesized Ni@γ-Fe$_2$O$_3$ NPs were investigated using transmission electron microscopy (TEM, Philips EM 420 with an acceleration voltage of 120 kV). Samples for TEM were prepared by placing a drop of dilute NP solution in hexane on a carbon coated copper grid. Low-resolution TEM images were recorded on a Philips EM420 microscope operating at an acceleration voltage of 120 kV. STEM data and ED patterns were obtained on a FEI Tecnai F30 S-TWIN with a 300 kV field emission gun.

X-Ray diffraction. XRD measurements were performed on a Bruker D8 Advance diffractometer equipped with a Sol-X energy-dispersive detector and operating with Mo Kα radiation. Crystalline phases were identified according to the PDF-2 database, using Bruker AXS EVA 10.0 software. Full profile fits on the basis of the crystal structural models[48,49] were performed with TOPAS Academic 4.1[50,51] applying the fundamental parameter approach.

Mössbauer spectroscopy and magnetic susceptibility measurements. Mössbauer spectra were obtained at room temperature, 150 K, 87.5 K and 4.2 K with a constant acceleration transmission Mössbauer spectrometer and a ^{57}Co (Rh) source. An α-Fe foil was used to calibrate the Mössbauer spectrometer in a velocity range of ±10 mm s^{-1}. Magnetic measurements were carried out using a Quantum Design MPMS-XL SQUID (superconducting quantum interference device) magnetometer.

Automated electron diffraction tomography (ADT)

Automated electron diffraction tomography (ADT) is a method for *ab initio* structure analysis of nanocrystals. ADT allows fine sampling of the reciprocal space by sequential collection of electron diffraction patterns while tilting a nanocrystal in fixed tilt steps around an arbitrary axis. Electron diffraction is collected in nano diffraction mode (NED) with a semi-parallel beam with a diameter down to 50 nm. For crystal tracking micro-probe STEM imaging is used. Full automation of the acquisition procedure allowed optimization of the electron dose distribution and therefore analysis of highly beam sensitive samples. Cell parameters, space group and reflection intensities can be determined directly within a reconstructed 3d diffraction volume using a dedicated software package (ADT3D). Intensity data sets extracted from such a volume usually show a high coverage and significantly reduced dynamical effects due to "off-zone" acquisition. The use of this data for "*ab initio*" structure solution by direct methods implemented in standard programs for X-ray crystallography is demonstrated. NED, automated diffraction tomography (ADT) and HRTEM were used for crystallographically characterizing the superparticles. Automated electron diffraction tomography (ADT) is a method for *ab initio* structure analysis of nanocrystals,[52,53] which allows fine sampling of the reciprocal space by sequential collection of electron diffraction patterns while tilting a nanocrystal in fixed tilt steps around an arbitrary axis. Electron diffraction is collected in nano diffraction mode (NED) with a semi-parallel beam with a diameter down to 20–50 nm.[54]

^{1}H NMR. ^{1}H NMR spectra (400 MHz) were recorded using a Bruker Avance III HD 400 apparatus operated at 400 MHz with a 5 mm BBFO-SmartProbe (Z-gradient) and an ATM as well as a SampleXPress 60 auto sampler. GPC measurements were performed in DMF (containing 0.25 g L^{-1} lithium bromide as an additive). An Agilent 1100 Series was used as an integrated instrument, including a PSS HEMA column (106/105/104 g mol^{-1}), a UV (275 nm) and a RI detector. Calibration was carried out using poly(ethylene glycol) standards purchased from Polymer Standards Service.

Results and discussion

Synthesis of Ni@γ-Fe$_2$O$_3$ superparticles

The synthesis of the Ni@γ-Fe$_2$O$_3$ superparticles with a central Ni nanoplate core (~100 nm) and γ-Fe$_2$O$_3$ (~30 nm) nanorods domains is illustrated in Fig. 1. In the first step, Ni nanoparticles were nucleated homogeneously *via* co-reduction by heating nickel acetate, Ni(ac)$_2$, in the presence of iron pentacarbonyl, Fe(CO)$_5$, at 120 °C. The emerging Ni nuclei transformed to Ni nanoplates (confirmed by examining aliquots at 140 °C) still significantly below the decomposition temperature (T = 180 °C) of Fe(CO)$_5$. In the final heating step at 180 °C γ-Fe$_2$O$_3$ nanorods grew epitaxially on the preformed Ni nanoplates. The products were precipitated and separated by centrifugation (9000 rpm, 10 min, RT).
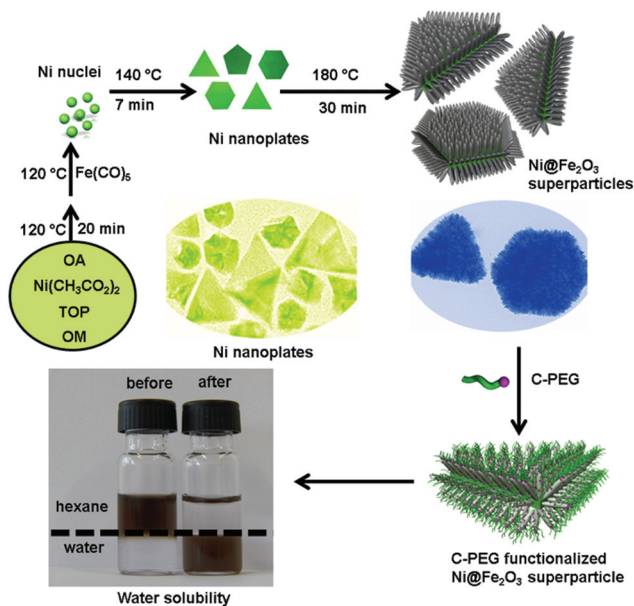
Fig. 1 Synthesis of Ni@γ-Fe$_2$O$_3$ superparticles. Initial Ni nuclei obtained by thermolysis of Ni(ac)$_2$ transform to Ni nanoplates with a Ni$_{1-x}$Fe$_x$ interlayer in the presence of Fe(CO)$_5$, from which highly oriented γ-Fe$_2$O$_3$ rods grow epitaxially (OM stands for oleylamine, TOP for tri-octyl-phosphine, and OA for oleic acid). The resulting Ni@γ-Fe$_2$O$_3$ superparticles are functionalized with a catechol-polyethylene glycol (C-PEG) ligand to achieve water solubility.

Polymer synthesis

The as-synthesized superparticles were functionalized using catechol-polyethylene glycol (C-PEG) polymer ligands[47] (Scheme S1†), which were characterized by ^{1}H NMR spectroscopy and GPC (Fig. S1 and 2†). The C-PEG ligands were synthesized *via* anionic ring opening polymerization of ethylene oxide (EO) starting from a protected catechol-initiator. This synthetic strategy allows a precise tailoring of the chain-length of PEG through the initiator to monomer ratio and guarantees well-defined polymers because of the living character of the polymerization.[47] A cartoon of a C-PEG functionalized Ni@Fe$_2$O$_3$ superparticle is shown in Fig. 1. It is worth mentioning that particles of this size (~200 nm) cannot be solubilized using low molecular weight C-PEGs. After functionalization the superparticles were easily dispersible in water; the dispersions were stable for several weeks.

Superparticle growth mechanism

The growth of the Ni@γ-Fe$_2$O$_3$ superparticles was monitored by taking "snapshots" at given time intervals using transmission electron microscopy (TEM). After ~6 minutes plate-like structures were formed (Fig. 2a and b). High-resolution transmission electron microscopy (HRTEM) images revealed that the smallest particles (20–30 nm) were polycrystalline, often displaying penta-twinned structures (Fig. 2a), whereas larger plate-like particles (30–80 nm) had a well-defined triangular morphology. EDX showed the particles to have a com-
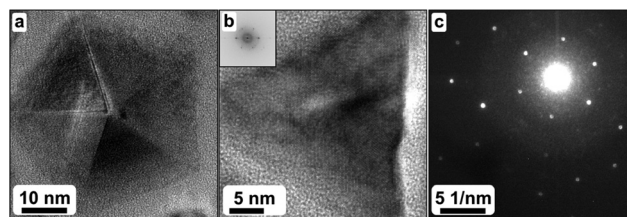

Fig. 2 Growth mechanism: Fe$_{0.05}$Ni$_{0.95}$ precursors after a reaction time of 5 minutes. (a) HRTEM of a pentagonally twinned particle. (b) HRTEM image and (c) NED of a single-crystal flat particle displaying a hexagonal pattern with *d*-distances of 2.2(1) Å.

position Fe$_{0.05}$Ni$_{0.95}$ (Fig. S3†). They were single crystalline (shown by HRTEM and nano-electron diffraction (NED)) with a hexagonal pattern and *d*-values of 2.2(1) Å (Fig. 2b and c). At this stage, all particles had a flat triangular or hexagonal habit in agreement with an earlier report by Leng *et al.*[55] and a composition of Fe$_{0.05}$Ni$_{0.95}$ as determined by NED, ADT and energy-dispersive X-ray spectroscopic EDX.

When heating slowly to 180 °C, γ-Fe$_2$O$_3$ nanorods started nucleating on the Fe$_{0.05}$Ni$_{0.95}$ cores. Their growth proceeded anisotropically (Fig. 3a). To show a better overview, an SEM image is provided Fig. S4.† The image further confirms hierarchical arrangements of nanodomains in three dimensional (3D) patterns. EDX line profiles taken across the superparticles showed the rods to consist of Fe$_2$O$_3$ nanorods decorating a core of metallic Ni plates containing a minor amount of Fe (Fig. 3b). The corresponding STEM image (Fig. 3c) confirms
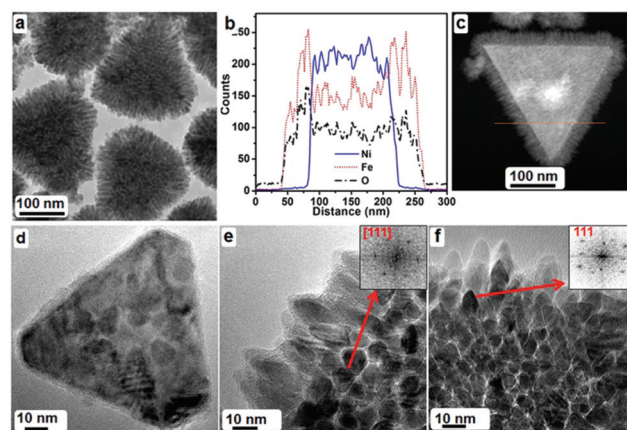

Fig. 3 Growth of Ni@γ-Fe$_2$O$_3$ superparticles. (a) Zoom of a superparticle showing preferential orientation of the rods growing on the large flat surfaces and the scattered orientation of the rods growing on the core side. (b) An EDX scan (along the red line) confirmed the elemental composition of the superparticle with the aid of a *z*-contrast image (STEM). (c) Corresponding Ni@γ-Fe$_2$O$_3$ superparticle. (d) HRTEM of a superparticle at an early stage with nucleated domains of [111] oriented Fe$_2$O$_3$. (e) HRTEM image of a superparticle showing rods growing on the main surface of the Ni plate and viewed along the main direction of growth, *i.e.* [111]. (f) HRTEM image showing rods growing on the side of the Ni plate with vector 111 pointing along out from the superparticle.
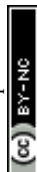
the presence of $Fe_{0.05}Ni_{0.95}$ cores and hierarchically grown Fe_2O_3 nanorods. Initially the rods covered only the flat surfaces of the $Fe_{0.05}Ni_{0.95}$ cores and grew perpendicular to the cores (Fig. 3d).

In Fig. S5† a *z*-contrast image from an upright standing plate gives a side view of the superparticles. The strong contrast difference between the Fe_2O_3 decoration and the very bright Ni plates was confirmed by energy-dispersive X-ray spectroscopic (EDX) line scan analysis. The average plate thickness was about 10 nm; this could be shown for many plates of different lateral size by tilting the sample. As the supercrystals kept growing, additional rods appeared on the side of the $Fe_{0.05}Ni_{0.95}$ cores with a less ordered orientation. The fully-grown nanorods were about 10 nm in diameter and about 30 nm in length (Fig. 3e). HRTEM images confirmed the main direction of the rod growth to be always [111]. Most nanorods developed orthogonally to the surface of the Ni plate, showing in projection a typical hexagonal base (Fig. 3e). Other rods grow on the lateral side of the Ni plate, with the [111] vector pointing out from the superparticle surface.

The size and density of the γ-Fe_2O_3 nanorods could be controlled by varying the concentration of the $Fe(CO)_5$ precursor in solution. The TEM images in Fig. 4a and b show that by reducing the concentration of $Fe(CO)_5$ the size and density of the γ-Fe_2O_3 nanorods decreased (Fig. 4a), whereas an increase of the $Fe(CO)_5$ concentration induced the formation of dense and almost 100 nm long γ-Fe_2O_3 nanorods (Fig. 4b). However, when $Fe(CO)_5$ was injected at 180 °C, *i.e.* the decomposition temperature of $Fe(CO)_5$, a mixture of Ni plates and iron oxide nanoparticles (Fig. S6a†) was obtained. Further increasing the injection temperature to 240 °C lead to the formation of core–shell nanoparticles, because the Ni cores had adopted already a spherical shape (Fig. S6b†). When the amount of $Fe(CO)_5$ was reduced to 10 μl, the reduction of the nickel precursor was incomplete, and agglomerated iron oxide nanostructures were formed (Fig. S6c†), whereas the injection of excess $Fe(CO)_5$ lead to the formation of $Ni@\gamma$-Fe_2O_3 superparticles with iron oxide nanorods ~100 nm long and also isolated iron oxide nanoparticles (Fig. S6d†). The reaction in the absence of $Fe(CO)_5$ did not allow a reduction of Ni as indicated by the
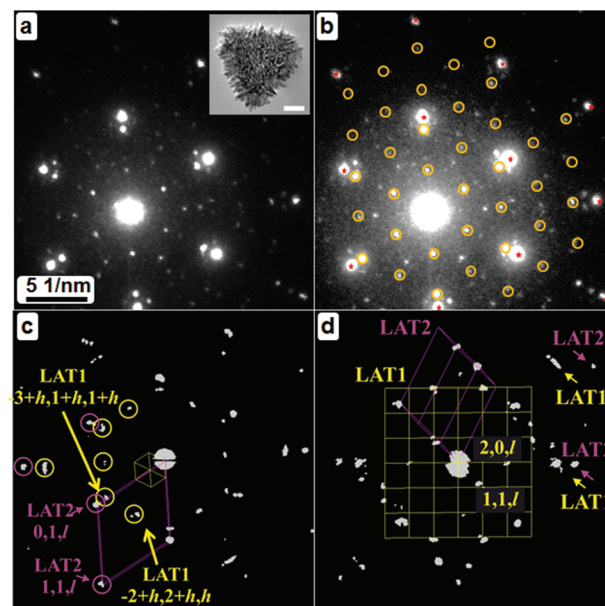
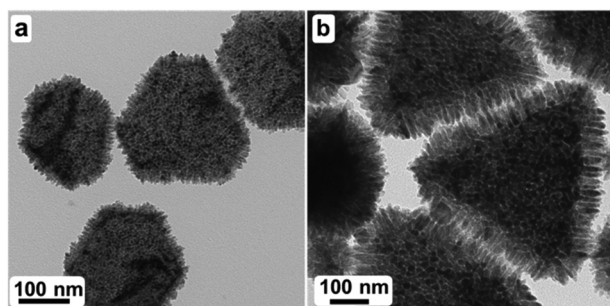**Fig. 5** NED and ADT characterization of mature $Fe_{0.05}Ni_{0.95}@\gamma$-$Fe_2O_3$ superparticles. (a) NED pattern from the particle inset (scale bar = 50 nm). (b) The pattern could be indexed with two hexagonal patterns with *d* values of 3.0(1) Å (in yellow) and 2.2(1) Å (in violet), respectively. (c) ADT 3D diffraction reconstruction viewed along the vertical and (d) along a lateral side. The two lattices identified by ADT are sketched in yellow (LAT1) and violet (LAT2).

color of solution even after heating to 180 °C for 30 min (Fig. S7†).

The superparticle formation is therefore clearly a hierarchical assembly, as the oxidation of Fe starts only after the Ni-based cores are fully developed. Selected area electron diffraction (SAED) patterns taken either from triangular or hexagonal superparticles could be fully described using two different lattices (Fig. 5a and b). One lattice is consistent with that already observed for the plate-like precursor, *i.e.* two *d* distances of 2.2(1) Å crossing at 60°. The second lattice is also hexagonal, with *d* values of 3.0(1) Å, and it is iso-oriented with respect to the first one.

Ni@γ-Fe₂O₃ superparticle structure

ADT[52,53] was used to obtain a three-dimensional diffraction reconstruction from four independent superparticles (Fig. 5c and d). The reconstructions were equivalent for triangular and hexagonal shapes. Besides diffuse scattering, presumably produced by randomly oriented γ-Fe_2O_3 rods, two single crystal lattices could be identified (Fig. 5). The first lattice (LAT1) corresponds to a face-centered cubic cell with *a* = 8.4(1) Å, consistent with the maghemite (γ-Fe_2O_3) cell. The second lattice (LAT2) corresponds to a primitive hexagonal cell with *a* = 2.55(5) Å and *c* = 6.2(1) Å. The orientation of the two lattices is correlated, as (111)* and (−211)* reciprocal vectors of LAT1 are respectively parallel to the (001)* and (100)* vectors of LAT2. Vectors LAT1(111)* and LAT2(001)* are perpendicular to the

Fig. 4 (a, b) In order to control the density and size of the γ-Fe_2O_3 domains the concentration of the $Fe(CO)_5$ was reduced (a) and increased (b).

plane of the Ni core, while vectors LAT1(−211)* and LAT2(100)* point to the vertexes of the triangles and vectors LAT1(−110)* and LAT2(110)* point to the vertexes of the hexagons (Fig. S8†).

The cubic lattice LAT1 is associated with the γ-Fe_2O_3 nanorods growing perpendicular to the surface of the $Fe_{0.05}Ni_{0.95}$ cores. They produce a single crystal-type pattern, because they have the same orientation. HRTEM images confirm the main direction of the rod growth to be always [111] (Fig. 3f). The hexagonal pattern LAT2 is associated with the triangular (or hexagonal) $Fe_{0.05}Ni_{0.95}$ cores. This lattice is commensurate with the face-centered cubic lattice of metallic Ni, with a ~3.6 Å, but the cubic symmetry is reduced by additional reflections at (1/3, 1/3, 1/3) and (2/3, 2/3, 2) (Fig. S9†). These additional reflections may be rationalized by a superstructure induced by the insertion of Fe in the Ni structure, or by a 2-fold rotational twinning of the Ni structure along [111]. The precision of ADT precision does not allow resolving the small deviations between the cell dimensions of Ni and $Fe_{0.05}Ni_{0.95}$.

The presence of maghemite (γ-Fe_2O_3, defect spinel) in the samples was confirmed by powder X-ray diffraction (P-XRD). The XRD patterns of the Ni@γ-Fe_2O_3 superparticles displayed broad Bragg maxima indicative of small crystallite sizes (Fig. 6a). Due to reflection broadening, reflection overlap between the Ni and the γ-Fe_2O_3 phase and the high similarity of the corresponding line-patterns a quantitative phase analysis was performed by full pattern profile analysis ("Rietveld refinement") to distinguish between all possible phases (γ-Fe_2O_3, magnetite (Fe_3O_4) and nickel ferrite ($NiFe_2O_4$)).[56,57] For the Ni nanoplate domains of the Ni@Fe_2O_3 superparticles

the crystallite sizes of 8(1) nm from the Rietveld refinement are marginally larger for Ni and considerably larger for γ-Fe_2O_3 (21(1) nm). The extra reflections not captured by the Rietveld refinement are due to silicon used as substrate. The Mössbauer spectrum of the Ni@Fe_2O_3 superparticles at 295 K (Fig. 6b) shows a superposition of wo magnetic sextetts with approximately equal intensities. The component with an isomer shift IS = 0.3(1) mm s^{-1} corresponds to maghemite with an average hyperfine magnetic field of 478 kOe.[58] A broad magnetic subspectrum with an average hyperfine magnetic field of 433 kOe and IS = 0.6(1) mm s^{-1} can be attributed to the interface region between the pure maghemite phase and the Ni substrate.

Physical properties

The magnetic properties of the Ni@γ-Fe_2O_3 superparticles extracted from the temperature-dependent magnetization and hysteresis curves are shown in Fig. 6c and d. The superparticles are ferrimagnetic at 5 K and superparamagnetic above room temperature. The magnetization curve in Fig. 6c exhibits saturation magnetization values of $2.96\mu_B$ at 5 K, a value prevailing the expected one of $2.40\mu_B$ for γ-Fe_2O_3 on a Ni substrate following from the estimation: $2/3 \times 3.33\mu_B + 1/3 \times 0.62\mu_B$, where $3.33\mu_B$ and $0.62\mu_B$ are saturation magnetizations for γ-Fe_2O_3[59] and metallic Ni.[60] This value is also much higher as compared to Ni@γ-Fe_2O_3 with heterodimer morphology ($2.45\mu_B$ at T = 5 K)[17] and core shell ($1.53\mu_B$ at T = 5 K) as shown in Fig. S10.† The ZFC magnetization increases monotonically with temperature and the FC magnetization shows no significant change. The splitting of the ZFC and FC curves reaches a crossing point around 302 K (Fig. 6d), indicating a blocking temperature above room temperature. The common orientation of the maghemite nanorods on the Ni core of the superparticles leads to a greatly enhanced magnetization because the anisotropy of the superparticles decreases the surface spin canting and disorder, thereby leading to enhanced magnetization. We do not consider inter-particle interactions to play a significant role, because the superparticles do not show aggregation (Fig. 3).

Conclusion

This work provides a general approach to a new type of magnetic nanocomposite with complex but well-defined mesoscopic architectures through "beaker epitaxy" of basic nanoobjects, *e.g.* for probing the exchange coupling between magnetic particle components at the nanoscale. ADT analysis in combination with Mössbauer spectroscopy indicates that tailoring the interface between the metal and metal oxide components by "alloying" is a key step to the formation of this new kind of colloidal superparticles with multiple well-defined supercrystalline domains under kinetic control. Atom diffusion is eliminated here as rate-limiting step, and only reaction parameters such as interface or precursor structure control the nucleation event.[61] The formation of phase separ-
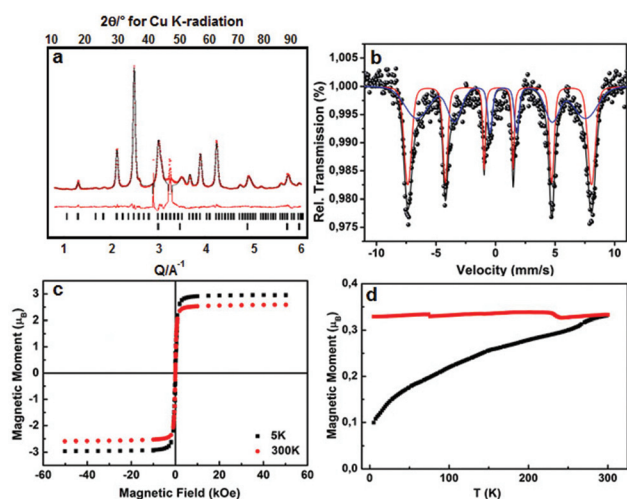

Fig. 6 Particle Characterization. (a) Quantitative phase analysis from the X-ray diffraction pattern of the Ni@γ-Fe_2O_3 superparticles (red dots: observed intensity, black line: calculated intensity, red line: difference curve; ticks mark the reflection positions of γ-Fe_2O_3 (upper) and elemental Ni (lower)), (b) ^{57}Fe Mössbauer spectra of Ni@γ-Fe_2O_3 superparticles at 295 K. (c, d) Magnetic hysteresis loops at 5 K and 300 K and temperature dependence of the magnetization in field-cooling (FC) and zero-field-cooling (ZFC) of Ni@γ-Fe_2O_3 superparticle heterodimers.
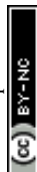
ated Ni@γ-Fe$_2$O$_3$ superparticles is highly unexpected, because Ni is not a noble metal and several stable ternary nickel oxides (e.g. nickel ferrite, NiFe$_2$O$_4$) are known, i.e. the nucleation temperature of these ternary phases is not reached under our experimental conditions.

The development of a controlled synthesis of nanocrystalline superparticles is relevant for several reasons: (i) The synthetic approach may be generalized for making nanocrystalline colloidal superparticles with other chemical compositions from organometallic precursors. (ii) The selective growth of the metal oxide nanorods is facilitated through the formation of Ni$_{1-x}$Fe$_x$ alloy and Fe$_{3-x}$Ni$_x$O$_4$ "buffer layers" (as shown by Mössbauer spectroscopy) at the interface between the Ni core and the γ-Fe$_2$O$_3$ rods within the Ni@γ-Fe$_2$O$_3$ superparticles that may serve to reduce strain in a regularly spaced arrangement on the Ni substrate as demonstrated by ADT. The miscibility of most d metals with each other in their elemental and oxide structures allows the fabrication of the buffer layer to be generalized. (iii) The properties of the nanocrystalline colloidal superparticles may be modified by "alloying" with other metals or by functionalization with organic molecules. Superparticles may be promising candidates for catalytic[17–19] or electrochemical[62] applications. Our functionalization strategy uses a well-defined catechol-functional PEG ligand with a tailored chain length and controlled molecular weight obtained from the living polymerization of EO.

We anticipate that our findings open many opportunities for assembling particles with complex, but well-defined mesoscopic architectures[63] and different magnetic, optical, or chemical properties. This could lead to new multifunctional materials or materials with enhanced performance for a wide range of potential (e.g. sensoric, catalytic) applications.[64,65]

Acknowledgements

Notes and references

1 H. C. Zeng, Acc. Chem. Res., 2013, 46, 226–235.

2 O. Chen, L. Riedemann, F. Etoc, H. Herrmann, M. Coppey, M. Barch, C. T. Farrar, J. Zhao, O. T. Bruns, H. Wei, P. Guo, J. Cui, R. Jensen, Y. Chen, D. K. Harris, J. M. Cordero, Z. Wang, A. Jasanoff, D. Fukumura, R. Reimer, M. Dahann, R. K. Jain and M. G. Bawendi, Nat. Commun., 2014, 5, 5093.

3 R. G. Chaudhuri and S. Paria, Chem. Rev., 2012, 112, 2373–2433.

4 M. Lattuada and T. A. Hatton, Nano Today, 2011, 6, 286–308.

5 M. N. Tahir, F. Natalio, M. A. Cambaz, M. Panthöfer, R. Branscheid, U. Kolb and W. Tremel, Nanoscale, 2013, 5, 9944–9949.

6 C. Huang, S. Wu, A. M. Sanchez, J. J. P. Peters, R. Beanland, J. S. Ross, P. Rivera, W. Yao, D. C. Cobden and X. Xu, Nat. Mater., 2014, 13, 1096–1101.

7 J. Y. Lao, J. G. Wen and Z. F. Ren, Nano Lett., 2002, 2, 1287–1291.

8 S. Park, S.-D. Seo, S. Lee, S. W. Seo, K.-S. Park, C. W. Lee, D.-W. Kim and K. S. Hong, J. Phys. Chem. C, 2012, 116, 21717–21726.

9 D. F. Zhang, L. D. Sun, C. J. Jia, Z. G. Yan, L. P. You and C. H. Yan, J. Am. Chem. Soc., 2005, 127, 13492–13493.

10 Y. Chen, C. Zhu, X. Shi, M. Cao and H. Jin, Nanotechnol., 2008, 19, 205603.

11 W. Zhou, C. Cheng, J. Liu, Y. Y. Tay, J. Jiang, X. Jia, J. Zhang, H. Gong, H. H. Hong and T. Yu, Adv. Funct. Mater., 2011, 21, 2439–2445.

12 U. K. Gautam, X. Fang, Y. Bando, J. Zhan and D. Golberg, ACS Nano, 2008, 2, 1015–1021.

13 M. Shang, W. Wang, W. Yin, J. Ren, S. Sun and L. Zhang, Chem. – Eur. J., 2010, 16, 11412–11419.

14 H. J. Fan, P. Werner and M. Zacharias, Small, 2006, 2, 700–717.

15 B. R. Martin, D. J. Dermody, B. D. Reiss, M. Fang, L. A. Lyon, M. J. Natan and T. E. Mallouk, Adv. Mater., 1999, 11, 1021–1025.

16 R. D. Robinson, B. Sadtler, D. O. Demchenko, C. K. Erdonmez, L. W. Wang and A. P. Alivisatos, Science, 2007, 317, 355–358.

17 B. Nakhjavan, M. N. Tahir, F. Natalio, M. Panthöfer, H. Gao, M. Dietzsch, R. Andre, T. Gasi, V. Ksenofontov, R. Branscheid, U. Kolb and W. Tremel, Nanoscale, 2012, 4, 4571–4577.

18 J. Jang, J. Chung, S. Kim, S. W. Jun, B. H. Kim, D. W. Lee, B. M. Kim and T. Hyeon, Phys. Chem. Chem. Phys., 2011, 13, 2512–2516.

19 C. Wang, H. Daimon and S. Sun, Nano Lett., 2009, 9, 1493–1496.

20 B. Nakhjavan, M. N. Tahir, M. Panthöfer, H. Gao, T. Gasi, V. Ksenofontov, R. Branscheid, S. Weber, U. Kolb, L. M. Schreiber and W. Tremel, Chem. Commun., 2011, 47, 8898–8900.

21 H. Yu, M. Chen, P. M. Rice, S. X. Wang, R. L. White and S. Sun, Nano Lett., 2005, 5, 379–382.

22 J. Kim, J. E. Lee, J. Lee, J. H. Yu, B. C. Kim, K. An, Y. Hwang, C. H. Shin, J. G. Park and T. Hyeon, J. Am. Chem. Soc., 2006, 128, 688–689.

23 I. Lee, J. B. Joo, Y. Yin and F. Zaera, Angew. Chem., Int. Ed., 2011, 50, 10208–10211.

24 M. Casavola, R. Buonsanti, G. Caputo and P. D. Cozzoli, Eur. J. Inorg. Chem., 2008, 837–854.

25 I. Schick, S. Lorenz, D. Gehrig, K. Fischer, S. Tenzer, H.-J. Schild, D. Strand, F. Laquai and W. Tremel, Beilstein J. Nanotechnol., 2014, 5, 2346–2362.

26 C. Wang, H. Daimon and S. Sun, Nano Lett., 2009, 9, 1493–1496.

27 Y. Wei, R. Klajn, A. O. Pinchuk and B. A. Grzybowski, *Small*, 2008, **4**, 1635–1639.

28 C. Xu, J. Xie, D. Ho, C. Wang, N. Kohler, E. G. Walsh, J. R. Morgan, Y. E. Chin and S. Sun, *Angew. Chem., Int. Ed.*, 2008, **47**, 173–176.

29 I. Schick, S. Lorenz, D. Gehrig, A.-M. Schilmann, H. Bauer, M. Panthöfer, K. Fischer, M. Schmidt, D. Strand, F. Laquai and W. Tremel, *J. Am. Chem. Soc.*, 2014, **136**, 2473–2483.

30 T. D. Schladt, T. Graf, O. Köhler, H. Bauer, K. Schneider, C. Herold, J. Mertins and W. Tremel, *Chem. Mater.*, 2012, **24**, 525–535.

31 G. Lopes, J. M. Vargas, S. K. Sharma, F. Beron, K. R. Pirota, M. Knobel, C. Rettori and R. D. Zysler, *J. Phys. Chem. C*, 2010, **114**, 10148–10152.

32 T. D. Schladt, M. I. Shukoor, M. N. Tahir, F. Natalio, K. Schneider, I. Ament, J. Becker, F. Jochum, S. Weber, P. Theato, L. M. Schreiber, C. Sönnichsen, H. C. Schröder, W. E. G. Müller and W. Tremel, *Angew. Chem., Int. Ed.*, 2010, **49**, 3976–3980.

33 I. Schick, D. Gehrig, M. Montigny, B. Balke, M. Panthöfer, A. Henkel, F. Laquai and W. Tremel, *Chem. Mater.*, 2015, **27**, 4877–4884.

34 C. Wang, C. Xu, H. Zeng and S. Sun, *Adv. Mater.*, 2009, **21**, 3045–3052.

35 L. Carbone and P. D. Cozzoli, *Nano Today*, 2010, **5**, 449–493.

36 C. Wang, W. Tian, Y. Ding, Y.-Q. Ma, Z. L. Wang, N. M. Markovic, V. R. Stamenkovic, H. Daimon and S. Sun, *J. Am. Chem. Soc.*, 2010, **132**, 6524–6529.

37 M. R. Buck, J. F. Bondi and R. E. Schaak, *Nat. Chem.*, 2011, **4**, 37–44.

38 B. Nakhjavan, M. N. Tahir, H. Gao, T. Schladt, K. Schneider, F. Natalio, I. Ament, R. Branscheid, S. Weber, H.-C. Schröder, W. E. G. Müller, U. Kolb, C. Sönnichsen, L. M. Schreiber and W. Tremel, *J. Mater. Chem.*, 2011, **21**, 8605–8611.

39 C. Xu, K. Xu, G. Gu, R. Zheng, H. Liu, X. Zhang, Z. Guo and B. Xu, *J. Am. Chem. Soc.*, 2004, **126**, 9938–9939.

40 M. N. Tahir, M. Eberhardt, P. Theato, S. Faiß, A. Janshoff, T. Gorelik, U. Kolb and W. Tremel, *Angew. Chem., Int. Ed.*, 2006, **45**, 908–912.

41 J. Sedo, J. Saiz-Poseu, F. Busque and D. Ruiz-Molina, *Adv. Mater.*, 2013, **25**, 653–701.

42 E. Amstad, T. Gillich, I. Bilecka, M. Textor and E. Reimhult, *Nano Lett.*, 2009, **9**, 4042–4048.

43 B. P. Lee, J. L. Dalsin and P. B. Messersmith, *Biomacromolecules*, 2002, **3**, 1038–1047.

44 J. Su, F. Chen, V. L. Cryns and P. B. Messersmith, *J. Am. Chem. Soc.*, 2011, **133**, 11850–11853.

45 M. S. Thompson, T. P. Vadala, M. L. Vadala, Y. Lin and J. S. Riffle, *Polymer*, 2008, **49**, 345–373.

46 B. Obermeier, F. Wurm, C. Mangold and H. Frey, *Angew. Chem., Int. Ed.*, 2011, **50**, 7988–7997.

47 V. S. Wilms, H. Bauer, C. Tonhauser, A. M. Schilmann, M. C. Müller, W. Tremel and H. Frey, *Biomacromolecules*, 2013, **14**, 193–199.

48 A. Taylor, *J. Inst. Metals*, 1950, **77**, 585.

49 C. A. Greaves, *J. Solid State Chem.*, 1983, **49**, 325–333.

50 A. Coelho, *TOPAS Academic V 4.1*, Coelho Software, Brisbane, AUS, 2007.

51 R. W. Cheary and A. A. Coelho, *J. Appl. Crystallogr.*, 1992, **25**, 109–121.

52 U. Kolb, T. Gorelik, C. Kübel, M. T. Otten and D. Hubert, *Ultramicroscopy*, 2007, **107**, 507–513.

53 U. Kolb, T. Gorelik and M. T. Otten, *Ultramicroscopy*, 2008, **108**, 763–772.

54 E. Mugnaioli, I. Andrusenko, T. Schüler, N. Loges, R. E. Dinnebier, M. Panthöfer, W. Tremel and U. Kolb, *Angew. Chem., Int. Ed.*, 2012, **51**, 7041–7045.

55 Y. Leng, Y. Li, X. Li and S. Takahashi, *J. Phys. Chem. C*, 2007, **111**, 6630–6633.

56 W. Kelm and W. Mader, *Z. Naturforsch.*, 2006, **61b**, 665–671.

57 C. Cavelius, K. Moh and S. Mathur, *Cryst. Growth Des.*, 2012, **12**, 5948–5955.

58 N. N. Greenwood and T. G. Gibb, *Mössbauer Spectroscopy*, Chapman and Hall Ltd, London, 1971.

59 H. Lueken, *Magnetochemie, Teubner Studienbücher*, 2000.

60 H. Danan, A. Herr and A. J. P. Meyer, *J. Appl. Phys.*, 1968, **39**, 669–670.

61 D. C. Johnson, *Curr. Opin. Solid State Mater. Sci.*, 1998, **3**, 159–167.

62 B. Oschmann, M. N. Tahir, F. Mueller, D. Bresser, I. Lieberwirth, W. Tremel, S. Passerini and R. Zentel, *Macromol. Rapid Commun.*, 2015, **36**, 1075–1082.

63 C. Feldmann, *Angew. Chem., Int. Ed.*, 2013, **52**, 7610–7611.

64 C. Burda, X. Chen and M. A. El-Sayed, *Chem. Rev.*, 2005, **105**, 1025–1102.

65 H. Goesmann and C. Feldmann, *Angew. Chem., Int. Ed.*, 2010, **49**, 1362–1395.